Characterization of glass fiber reinforced polymer via Digital Volume Correlation: Quantification of strain activity and damage growth

Ana Vrgoč, Zvonimir Tomičević, Benjamin Smaniotto, François Hild

Characterization of glass fiber reinforced polymer via Digital Volume Correlation: Quantification of strain activity and damage growth

Ana Vrgoč[1,2], Zvonimir Tomičević[1,*], Benjamin Smaniotto[2], François Hild[2]

[1] *University of Zagreb, Faculty of Mechanical Engineering and Naval Architecture*
Ivana Lučića 5, 10002 Zagreb, Croatia
[2] *Université Paris-Saclay, CentraleSupélec, ENS Paris-Saclay, CNRS*
LMPS - Laboratoire de Mécanique Paris-Saclay, 91190 Gif-sur-Yvette, France

Abstract

Strain and damage distributions within a dogbone specimen containing a rectangular notch were assessed *in-situ* via X-Ray Computer Tomography coupled with Digital Volume Correlation. The specimen cut from a continuous glass fiber mat reinforced polyester resin composite plate was subjected to cyclic tensile loading. The strain-damage interplay was evaluated by analyzing major eigen strain and correlation residual fields. The horizontal strained band emanating from the notch root was present from the beginning of loading. The final failure proceeded along this strained band. The first cracks did not initiate in the notched region, despite high strain gradients. Strain activity and damage growth were quantified by analyzing the cumulative probabilities of major eigen strains. The comparison was made between the notched region and the remaining part of the inspected specimen. It is shown that, although the mean levels were higher in the notched region, the standard deviations of the major eigen strain distributions were higher in the remaining part of the specimen.

Keywords: Polymer matrix composite, Digital Volume Correlation, Damage growth, Correlation residuals, Strain fields

1. Introduction

The ever-increasing application of fiber-reinforced polymers (FRP) in various industry branches is justified by their advantageous properties (*e.g.*, high stiffness to weight ratio) compared to conventional engineering materials [1]. The failure of such materials is induced by various damage mechanisms initiating at different scales (micro-, meso- and

*Corresponding author
Email address: zvonimir.tomicevic@fsb.hr (Zvonimir Tomičević)

macroscale) [2]. Due to the likely activation of different damage mechanisms and their interaction, comprehensive analyses of damage phenomena call for advanced techniques for damage detection and monitoring.

Damage phenomena within the material bulk can be experimentally assessed employing X-Ray Computed Tomography (XCT). The latter has been extensively used to quantify damage growth within specimens subjected to different loading regimes by processing 3D images [3, 4, 5, 6]. However, this approach enabled only microstructural changes to be assessed, *i.e.*, the bulk kinematics was not determined, nor was it related to microstructural features. This limitation can be overcome with Digital Volume Correlation, which aims at measuring displacements and calculating strains both on the surface and in the material bulk by correlating two scans acquired at different stages [7, 8, 9]. As such, this full-field measurement technique complements XCT analyses. Local approaches to DVC, which split the inspected Region of interest (ROI) into smaller sub-volumes that are registered independently (*i.e.*, the displacement continuity between adjacent sub-volumes is not ensured), are employed in the majority of existing studies on FRP [10, 11, 12]. In a recent work [13], it was shown that the regions exhibiting high strains also corresponded to damage inception areas within a short fiber reinforced polymer composite. A strain threshold was used to isolate highly strained regions. These "hot spots" were compared to damage inception areas manually detected in the 3D images. Even though the proposed approach resulted in a reduction of time and computational resources needed to inspect damaged zones (as DVC strain fields provided the indication of damage inception areas), the overall outcome still depended on the heterogeneity of the strain fields and active damage mechanisms.

Global approaches based on finite element (FE) discretizations were recently introduced [14, 15]. They generally assume the continuity of displacement fields. One of the major advantages of such approaches is the accessibility of correlation residuals that correspond to the gray level difference between the reference volume and the volume of the deformed material corrected by the measured displacement field [7]. As the gray level conservation is the underlying hypothesis of DVC [16, 17, 9], correlation residuals are used for registration quality inspection (*i.e.*, when checking the convergence of the algorithm). As damage phenomena deteriorate gray level conservation, discontinuities and damaged zones for converged displacement fields can be unveiled by studying the correlation residual fields [18, 7, 19]. The quantification of strained areas and damage growth, as well as the analysis of strain-damage interaction, was thus provided within a single framework.

The research performed herein considers the quantification of strain activity and damage growth in a dogbone specimen subjected to cyclic tensile loading and simultaneously imaged in an XCT scanner. The investigated specimen was cut from a continuous glass fiber mat reinforced polyester resin composite plate, and contained a rectangular notch machined

to induce high strain gradients. The bulk displacements were measured with FE-based DVC, which enabled for the calculation of 3D strain maps. The strained band activity and damage growth were quantified by analyzing the cumulative probabilities of major eigen strain distributions extracted during the prescribed loading history. Two quantities are analyzed, namely, mean levels and standard deviations of the corresponding distributions.

The present paper is organized as follows. First, the properties and fabrication procedure of the investigated composite material are presented, followed by a brief description of regularized FE-based DVC. The investigated specimen geometry is presented together with the employed mechanical and imaging setup. Prior to loading the specimen, two scans were acquired in the undeformed state to evaluate measurement uncertainties. Next, the results of volume registrations are discussed. Last, the quantification of strain activity and damage growth within the investigated specimen is performed.

2. Material and experimental setup

The material of the single notched specimen is a polyester resin reinforced with continuous glass fiber mat. It was produced by manual lay-up followed by compression molding. The laminate consisted of 12 plies of R-glass fiber mat. The composition (in volume fraction %) was 40% of fibers, 55% of matrix and, as vacuum was not applied during molding, the volume fraction of air voids was equal to 5%. The enhanced contrast between the constituents (in this specific case, between matrix, fibers and air voids, as shown in Fig. 1(a)) makes the investigated material suitable for DVC as it relies on natural contrast [7].

The dogbone specimen geometry is shown in Fig. 1(a). The thickness of the specimen was 5.2 mm, while the notch depth and width were equal to 1.6 mm and 0.6 mm, respectively. The studied specimen was subjected to cyclic tensile loading with the TTC Deben testing machine, while being simultaneously imaged in the X50+ scanner (North Star Imaging) of LMPS. The test comprised of 4 loading cycles corresponding to 25%, 50%, 75% and 90% of specimen failure strength ($\sigma_m = 135$ MPa), as shown in Fig. 1(b). The stroke velocity was equal to 4 µm/s. After applying each loading/unloading step, the specimen was scanned while rotating about the tomographic axis. 3D images (encoded as 8-bit deep gray levels) were reconstructed from the collected radiographs captured at equally spaced angles by using a filtered back-projection algorithm [20], and no additional filtering was applied. The size of the ROI focused on the thinned ligament was $680\times465\times1001$ voxels (Fig. 1(a)). The scanning parameters are given in Appendix A (Table A.1). The first scan (0) was acquired with high quality (HQ) scanning parameters. As it resulted in low noise levels, it was considered as the reference for evaluating measurement uncertainties and performing subsequent correlation analyses. However, this acquisition required 2 h to be completed. Thus, to conduct the experiment in a reasonable time, as well as to mitigate *e.g.* relaxation

phenomena, the number of averaging frames for all subsequent acquisitions was reduced to 1 (continuous scanning parameters, see Table A.1). Such parameters led to 4 min acquisitions. After acquiring the reference scan, 10 additional scans were acquired during the loading procedure. The physical size of one voxel was 14.6 µm.

The inspected ROI was discretized with first-order tetrahedral elements tailored to the actual specimen geometry. The average element length was 11 voxels. It was *a priori* assumed that the notch would induce high strain gradients and, consequently, damage phenomena would concentrate in that area. Thus, the mesh was refined in the notched region, *i.e.*, the average element lengths of the notched region and the remaining part of the ROI were 8 voxels and 14 voxels, respectively. The total number of degrees of freedom (DOFs) was 68,451 for the measured displacement field.

3. Digital Volume Correlation

The present section outlines the basic principles of regularized FE-based DVC. Next, the measurement uncertainties are evaluated by correlating two scans of undeformed stages. These scans (0 and 00) were acquired prior to prescribing any load.

3.1. Registration principle

Global DVC employed herein is a full-field measurement technique enabling for displacement measurements and calculation of strain maps within the bulk of investigated materials [7, 8, 9]. This technique relies on matching the gray levels between the reconstructed volume of the reference configuration $f(\mathbf{x})$ (where $\mathbf{x}$ denotes the voxel location) and a series of images $g(\mathbf{x})$ of deformed configurations. Thus, the gray level conservation is assumed to relate two reconstructed volumes

$$f(\mathbf{x}) = g(\mathbf{x} + \mathbf{u}(\mathbf{x})), \tag{1}$$

where $\mathbf{u}$ is the measured displacement field. As the tomographic technique causes deviations due to acquisition noise and reconstruction artifacts, the conservation of gray levels cannot be satisfied in real applications. Thus, the aim of the correlation procedure is to minimize the sum of squared differences over the ROI with respect to the sought displacement amplitudes [14]

$$\Phi_c^2 = \sum_{\mathrm{ROI}} \varphi_c^2(\mathbf{x}), \tag{2}$$

where φ_c defines the gray level residual field

$$\varphi_c(\mathbf{x}) = f(\mathbf{x}) - g(\mathbf{x} + \mathbf{u}(\mathbf{x})). \tag{3}$$

As an FE-based approach was employed in the present study, the global residual was minimized with respect to the unknown degrees of freedom when the displacement is written as

$$\mathbf{u}(\mathbf{x}) = \sum_n u_n \mathbf{\Psi}_n(\mathbf{x}), \tag{4}$$

where u_n are nodal displacements, and $\mathbf{\Psi}_n$ the corresponding FE shape functions. Thus, the displacement field is regularized with a continuity requirement *a priori* assumed for the kinematic solution. Additional mechanical regularization acting as a low-pass displacement filter may be implemented in the correlation procedure.

3.2. Mechanical regularization

In the present work, mechanical regularization based on the equilibrium gap in linear elasticity was employed. Such an approach considers the L_2 norm of the unbalanced nodal forces for bulk degrees of freedom (DOFs) and traction-free surfaces (Neumann DOFs) [21]

$$\Phi_m(\{\mathbf{u}\}) = \{\mathbf{u}\}^\top [\mathbf{K}_m]^\top [\mathbf{K}_m] \{\mathbf{u}\}, \tag{5}$$

where Φ_m is the equilibrium gap function, and $[\mathbf{K}_m]$ the partial stiffness matrix for bulk and Neumann DOFs. As the external forces are not known, this premise is not valid for the remaining (Dirichlet) DOFs [21, 22]. An additional penalty term is employed for these nodes

$$\Phi_S(\{\mathbf{u}\}) = \{\mathbf{u}\}^\top [\mathbf{K}_S]^\top [\mathbf{L}] [\mathbf{K}_S] \{\mathbf{u}\}, \tag{6}$$

where $[\mathbf{K}_S]$ is the partial stiffness matrix for Dirichlet nodes, $[\mathbf{L}]$ the discrete Laplace-Beltrami operator, and $\{\mathbf{u}\}$ the column vector gathering the nodal displacements associated with the discretized displacement field $\mathbf{u}$. The total cost function Φ_t consists of a linear combination of DVC cost function Φ_c, equilibrium gap Φ_m, and penalty term for the gradient of normal tractions Φ_S

$$\Phi_t(\{\mathbf{u}\}) = \frac{\omega_c}{\omega_t}\widehat{\Phi}_c(\{\mathbf{u}\}) + \frac{\omega_m}{\omega_t}\widehat{\Phi}_m(\{\mathbf{u}\}) + \frac{\omega_S}{\omega_t}\widehat{\Phi}_S(\{\mathbf{u}\}), \tag{7}$$

with

$$\begin{aligned} \widehat{\Phi}_c(\{\mathbf{u}\}) &= \Phi_c(\{\mathbf{u}\})/(\{\mathbf{v}\}^\top [\mathbf{M}] \{\mathbf{v}\}), \\ \widehat{\Phi}_m(\{\mathbf{u}\}) &= \Phi_m(\{\mathbf{u}\})/\Phi_m(\{\mathbf{v}\}), \\ \widehat{\Phi}_S(\{\mathbf{u}\}) &= \Phi_S(\{\mathbf{u}\})/\Phi_S(\{\mathbf{v}\}). \end{aligned} \tag{8}$$

In Equation (8), the column vector $\{\mathbf{v}\}$ gathers the nodal displacements associated with a shear wave of wavevector $\mathbf{k}$ [21], and the weighting terms are related to corresponding

regularization lengths ℓ

$$\omega_c = 1, \qquad \omega_m = (\ell_m|\mathbf{k}|)^4, \qquad \omega_S = (\ell_S|\mathbf{k}|)^4, \tag{9}$$

such that

$$\omega_t = \omega_c + \omega_m + \omega_S. \tag{10}$$

The weights associated with mechanical regularization are varied by changing the regularization lengths. When FE-based DVC is employed, the regularization is activated for any length ℓ greater than the characteristic element length. Mechanical regularization penalizes high-frequency noise features and enforces smoothness of measured fields. Gains in measurement uncertainty can be achieved, and convergence of the correlation algorithm is enhanced [23, 7, 21].

The volumes acquired during the *in-situ* test were analyzed via regularized FE-based DVC implemented within the Correli 3.0 framework [24]. One of the major advantages of global DVC is the availability of correlation residual maps φ_c for each analyzed volume. These residuals provide useful information to detect damage inception and growth at the voxel scale. As the displacement fields are assumed to be continuous within the investigated ROI, higher values indicate local violations to gray level conservation, and thus reveal damaged zones [7, 8, 9]. In addition, global approaches based on finite element discretizations can be directly linked with numerical simulations of mechanical problems [25].

3.3. Selection of regularization length

The selection of the regularization length was conducted by correlating HQ scan 0 with scans 00 and 08 (corresponding to the peak force of the last loading cycle prior to specimen failure). Series of analyses were run with different bulk regularization lengths ℓ_m, while the regularization length for Dirichlet nodes ℓ_S was set to 64 vx. The reason for keeping ℓ_S constant was to lower displacement fluctuations on surfaces that may be used to drive numerical simulations with measured (Dirichlet) boundary conditions. The next DVC calculation was performed with ℓ_m divided by two, with as initial guess the displacement field at convergence of the previous calculation (*i.e.*, root mean square of the displacement correction between two iterations less than 10^{-4} vx). This relaxation procedure [22] was performed until ℓ_m was less than the mean element length (*i.e.*, no mechanical penalization).

The quality of regularized registration was evaluated by calculating mechanical residuals Φ_m and the root mean square (RMS) of the gray level residuals φ_c. Figure 2(a) shows that by increasing the regularization length, a significant decrease of mechanical residuals was observed. For scan 00, the RMS gray level residuals remained essentially constant especially for bulk regularization lengths greater than 64 vx. An increase in gray level residuals with the bulk regularization length was more pronounced for scan 08. This effect stems

from the fact that scan 08 was acquired at the peak of the last loading cycle prior to specimen failure, thus damage (which impaired gray level conservation) was expected to occur for high regularization lengths. Yet, even for scan 08, this increase was small. The variation of the regularization length did not have a significant influence on the correlation residuals (*i.e.*, on the quality of the registration). Conversely, the mechanical residuals varied significantly with the regularization lengths. In strongly regularized solutions, high spatial frequencies were smeared out, resulting in smooth displacement and strain fields. For scan 00, the mechanical residuals could be decreased at will by increasing the regularization length. Conversely, for scan 08, they leveled off when $\ell_m > 64$ vx, thereby indicating that the strain fluctuations should not be filtered out. According to the observed trends, employing a bulk regularization length ℓ_m of 64 vx and an identical regularization for Dirichlet nodes (*i.e.*, $\ell_S/\ell_m = 1$) was selected for the DVC analyses reported herein.

In regularized DVC, the mesh size can be made very small [16] and the uncertainties are then controlled by the regularization lengths once greater than the element size [26, 27]. This effect is observed in Fig. 2(b) when the DVC uncertainties were assessed by correlating scans 0 and 00. The DVC uncertainties correspond to the standard deviations (Std) of measured nodal displacements (after subtraction of rigid body motions). The strain uncertainty was calculated as the standard deviation of nodal values of major eigen strains. A decrease in regularization lengths resulted in an increase of standard measurement uncertainties, as the spurious fluctuations were less filtered out. This increase was more pronounced for regularization lengths less than 64 vx. The change in standard strain uncertainties was more pronounced as usually observed [28]. These remarks further justify the choice of employing ℓ_m equal to 64 vx.

The assessed measurement uncertainties (when employing bulk and surface regularization length equal to 64 vx) are reported in Table 1, together with the RMS correlation residuals Φ_c over the inspected ROI. They are related to intrinsic artifacts of the tomographic technique (*e.g.*, image noise, ring artifacts, spurious motions during scanning [7]), while an additional source of uncertainty was due to the fact that scans of different qualities were correlated (Table A.1). The reported values were deemed sufficiently low, and correspond to limits above which the mechanical signal is distinguished from noise.

4. Results

In this section, the results of the DVC analyses are presented. They all converged, *i.e.*, the RMS displacement increment between two iterations became less than 10^{-4} vx. First, the thresholded major eigen strain fields and correlation residual maps are analyzed to study strain-damage interactions. The absolute range of the correlation residual fields was chosen to be between 50 and 120 gray levels. As such, all estimated levels that fell outside

that specified range originated from mechanical causes. Damage initiation and growth was detected from local increases in correlation residuals (attributed to the violation of the gray level conservation and displacement continuity associated with the tetrahedral mesh). Last, the quantification of damage growth was performed by analyzing the cumulative probabilities of major eigen strain distributions extracted during the prescribed loading history. Two additional quantities are analyzed, namely, mean levels and standard deviations of the corresponding distributions.

4.1. Major eigen strain fields and correlation residual maps

Figure 3 shows the major eigen strain fields calculated for the scans acquired during the prescribed loading history (Fig. 1(b)). The cycle-wise loading was especially interesting in terms of activation and deactivation of strained bands. When complemented with correlation residual fields (Fig. 6), such an analysis enabled for the study of strain-damage interactions.

The cyclic strain fields displayed complex patterns, *i.e.*, the formation of multiple strained bands. The presence of an inner, horizontal strained band emanating from the notch root was first observed for scan 01 (Fig. 3(b)). This band already extended through the whole ligament area. As the loading levels became higher, several strained bands appeared within the investigated specimen (some of which originated from the notched root, while additional strained areas appeared on the specimen ligament edges). In spite of high strain gradients in the notched region, the observed strained bands experienced an increase of strain levels due to the prescribed loading. This remark implied that the investigated material was notch-insensitive [29].

In addition to the major eigen strain fields, the ε_{xx}, ε_{yy} and ε_{zz} strain fields of scan 08 (corresponding to the last loading cycle prior to specimen failure) are shown in Fig. 4. The ε_{xx} strain field was mainly homogeneous, except in the vicinity of the notch root where high gradients occurred. Conversely, the strain field in the through-thickness direction (ε_{yy}) was not uniform but exhibited strained bands (on the notch-free ligament edge), while a second strained band originated from the notch root and propagated below it reaching the ligament edge. It is worth noting that the final failure proceeded along the early, horizontal strained band. Yet, an additional crack branch appeared on the front specimen surface, and it corresponded to the strained band visible in the ε_{yy} strain field. High strain gradients were also observed close to the notch root near the front specimen surface ($y = 105$ vx). These gradients decreased when approaching the rear specimen surface ($y = 410$ vx). Last, the ε_{zz} strain field (corresponding to the loading direction) was very heterogeneous. The dominant, and essentially horizontal, strained band is visible, as well as the band emanating from the notch root and propagating below it toward the notch-free ligament edge. High strain

gradients are apparent within the notched region. From Fig. 4, it is concluded that the main contribution to the heterogeneity of the strain fields stemmed from ε_{yy} and ε_{zz} strains.

To further investigate the premise of notch-insensitivity, profiles of ε_{zz} strain averaged through the sample thickness ($y-$direction) in the slice $z = 538$ vx (corresponding to the notch mid-plane) are displayed in Fig. 5. These strain profiles were computed for the loaded (*i.e.*, 01, 03, 05, 07 and 08) scans. Very high strain levels and gradients developed at the notch root ($x = 474$ vx). Yet, they did not lead to premature failure. For all analyzed scans, the strain levels decreased when approaching the notch-free ligament edge ($x = 50$ vx). With an increase in prescribed load, the strains also increased outside of the notched region, despite high strain gradients at the notch root. The observed trends demonstrate the ability of the studied material to sustain very high strain levels and gradients within notched regions, and still undergo increases in strain levels within the remaining ROI.

The presented strain fields are complemented with the analysis of correlation residual maps to investigate strain-damage interplay. For scan 00, the correlation residual map exhibited very low levels homogeneously distributed within the ROI. The presence of a ring artifact in the center of the specimen was revealed not only for this scan, but for all subsequent acquisitions. This feature proves that the registrations were successful, *i.e.*, the initial differences between gray level volumes decreased to the noise level except where this phenomenon occurred. If the ring artifact had vanished, it would have meant that the algorithm tracked ring artifacts and not the underlying kinematics of the investigated specimen. It is also worth remembering that the gray level residuals serve as correlation quality inspection tool. As damage growth impaired gray level conservation (being the underlying hypothesis of global DVC employed in the present work) and consequently DVC convergence, the correlation residuals also provided the means for damage detection in the zones where the displacement continuity requirement was not met.

The first localized phenomena appeared near the unnotched ligament edge for scan 03, *i.e.*, at the peak of the second loading cycle (marked with the blue circle in Fig. 3(d)). As the remaining part of the investigated ROI displayed sufficiently low values (proving that the kinematics was well captured), it was concluded that the first cracks initiated, thereby indicating the influence of specimen machining. It is important to highlight that damage did not initiate in the notched region (in spite of high strain gradients), which further contributed to the hypothesis of notch-insensitivity. Yet, subsequent unloading led to damage deactivation due to crack closure (Fig. 6(e)). With the increase in load levels, numerous damaged zones appeared within the material bulk (marked with blue and red circles in Fig. 6(f)). The occurrence of damaged zones within the notched region was first observed for scan 05 (marked with the red rectangular prism in Fig. 6(f)). However, for scan 06 acquired in the unloaded stage, the cracks in the notched region were closed, while damage in

the remaining part of the ROI was still active. For scans 07 and 08, the previously observed damaged zones were once again active, as well as additional cracks appeared within the inspected ROI (marked with green and purple circles in Fig. 6(h-i). Once again, the subsequent unloading yielded damage deactivation (*i.e.*, crack closure) in the notched region, while damage in the remainder of the ROI was more pronounced.

From the reported major eigen strain fields and correlation residual maps, several conclusions can be drawn. First, even though the major eigen strain field is heterogeneous from the beginning of loading (*i.e.*, the formation of a horizontal strained band was unveiled for scan 01, see Fig. 3(b)), damage growth was not detected until the peak of the second loading cycle (scan 03, see Fig. 3(d)). If damage did occur, it remained very low and at a scale lower than the scan resolution [30]. Second, the first cracks initiated and propagated near the unnotched specimen ligament edge, in spite of high strain gradients in the notched region. This phenomenon was assumed to be caused by the specimen machining. In addition, compared to the notched region, damage in the remaining part of the ROI was more pronounced. It is important to highlight that the final failure of the investigated material proceeded along the horizontal strained band present from the beginning of the loading history. These remarks exemplify the notch-insensitivity of the investigated composite material [29]. To further investigate this hypothesis, damage growth and major eigen strains are quantified in the following section.

4.2. Quantification of strain activity and damage growth

In this section, cumulative probabilities of major eigen strains (ε_1) are analyzed to quantify strain activity and damage growth within the investigated specimen. Two quantities are analyzed, namely, mean levels and standard deviations of the corresponding distributions. The comparison is made between the notched region and the remaining part of the inspected ROI (see Fig. 1(a)) to investigate notch-insensitivity of the studied composite. To ensure better visualization, the cumulative probabilities of major eigen strain distributions are first analyzed cycle-wise, and their range was limited to 0.03.

The comparison of cumulative probabilities of major eigen strains between the notched region and the remainder of the ROI is shown in Fig. 7. For the scan acquired in the reference configuration (Fig. 7(a)), the reported major eigen strains were distributed within the range of measurement uncertainties (Table 1). The cumulative plots of both inspected regions exhibit identical slopes. Thus, the distribution of scan 00 extracted for the remaining part of the ROI is added to all subsequent plots to track the accumulation of permanent strains, as well as the initiation and opening of mesocracks. Even in the first loading cycle (scan 01), the major eigen strains within the notched region were higher than those of the remainder of the ROI (Fig. 7(b)). Thus, strain concentrations had already set in from the beginning of the prescribed loading history. Subsequent specimen unloading led to permanent

strains in the notched region *i.e.*, the cumulative probability of the corresponding region was shifted to the right compared to the probability of the remaining part of the ROI, as shown in Fig. 7(c). The latter one was distributed within the range of measurement uncertainties. Thus, no permanent strains were observed after the first loading cycle outside the notched region.

At the peak of the second loading cycle (scan 03) the strain levels within the whole ROI increased (Fig. 7(d)). This effect was more pronounced for the notched region, as the corresponding cumulative probability was significantly shifted to the right (compared to the distribution of the remaining part of the ROI) due to high strain gradients observed in the notched region. Yet, they did not lead to premature failure. For scan 04, the offset between the cumulative probabilities was due to the accumulation of permanent strains within the notched region (Fig. 7(e)). Still, permanent strains were not observed in the remaining part of the ROI. Yet, damage did not initiate in the notched region at this stage (Fig. 6(d)), whereas the first mesocracks appeared near the notch-free ligament edge due to specimen machining, as shown in Fig. 6(d).

The shift of cumulative probabilities to higher values was even more pronounced when the specimen was cycled to 75% of its failure strength (scan 05), see Fig. 7(f). Again, high strain gradients were induced in the notched region. After the specimen was unloaded (scan 06), the major eigen strains were higher than those of scan 04 (Fig. 7(g)). Thus, the accumulation of permanents strains was present in both parts of the ROI. It is interesting to note that, for scan 06, the shift of cumulative distribution toward higher strains was again more pronounced for the notched region. Yet, the first mesocracks occurring in the vicinity of the notch root closed at this stage. Conversely, damaged zones near the specimen ligament edges remained active, as shown in Fig. 6(g). This trend exemplifies the notch-insensitivity of the studied material, namely, damage outside the notched region was more pronounced even when the specimen was unloaded, in spite of high strain gradients induced in the notched area.

Figures 7(h-j) show the cumulative probabilities of major eigen strains extracted for the last loading/unloading cycle prior to specimen failure (*i.e.*, scans 07, 08 and 09). At the peak of the fourth loading cycle (scans 07 and 08), a significant increase of strain levels was observed in the notched region. Yet, they did not cause premature specimen failure, and the strain levels within the strained bands observed outside the notched region increased as load levels became higher (Fig. 3(h-i)). The cumulative probabilities for scan 09 acquired in the unloaded configuration revealed that during the prescribed loading, the accumulation of permanent strains was more pronounced in the notched region. Yet, the strain levels increased within the remainder of the ROI with higher load levels. This effect proves that the impact of strained band and damage activity outside the notch on the final failure was

stronger compared to the geometric effect induced by the notch and/or specimen machining.

The strained band activity and damage growth within the single notched specimen were further quantified by analyzing the mean and standard deviation of major eigen strain distributions. Figure 8 shows the change of mean levels of major eigen strain distributions and their fluctuations (*i.e.*, error bars corresponding to the standard deviation). The later ones are reported in Table 2. The mean levels of major eigen strain distributions extracted from the notch region were higher compared to those in the remainder of the ROI even for the first loading cycle (scan 01) due to the high strain gradients. The reported mean levels also prove that permanent strains accumulated within the notched region after the first loading cycle (scan 02). For the remainder of the ROI, the accumulation of permanent strains were induced later on. Conversely, Std(ε_1) levels of the notched region were lower than those of the remainder of the ROI. This phenomenon was first observed for scan 01. Cycling the specimen up to 25% of its failure strength led to the occurrence of a horizontal strained band originating from the notch root, as well as strained areas on the specimen ligament edges (Fig. 3(b)), in spite of high strain gradients induced in the notch region. Furthermore, the first mesocracks emerged close to the notch-free ligament edge (Fig. 6(d)), which is reflected in an increase of the fluctuations for scan 03. Upon subsequent unloading (scan 04), the fluctuations again decreased to the level of scan 00, *i.e.*, crack closure and damage deactivation occurred (Fig. 7(e)). For scan 05, a significant increase of Std(ε_1) was observed for both parts of the ROI. The reported levels are well above the strain uncertainties reported in Table 1. These fluctuations were due to the pronounced strain activity within the inspected specimen (Figure 3(f)), as well as the opening of mesocracks revealed in the corresponding residual map (Fig. 6(f)). Furthermore, a substantial increase of fluctuations was observed for scans 07 and 08 due to an increase of strain levels within the inspected ROI, as well as opening of existing cracks and the inception of additional damaged zones (Fig. 6(h-i)). Last, the fluctuations of scan 09 reveal that permanent strains accumulated, as well as notable amount of damage during the prescribed loading history. The analysis of mean levels and standard deviation of major eigen strain distributions of the single notched specimen further proved that, even though high strain gradients were induced in the notch region, the strain activity within the remaining part of the ROI significantly contributed to the final failure. The strain levels outside of the notched region gradually increased as the load levels became higher, and the damage activity was more pronounced in that area. These observations once again explain the notch-insensitivity of the investigated composite.

The cumulative probabilities of major eigen strains of the single notched specimen confirmed that the first cracks did not initiate in the notched region, despite the high strain activity. Damage phenomena were first observed near the ligament edge. The impact of specimen machining was assumed to be its cause. The first cracks appeared in the vicinity

of the notch root at the peak of the third loading cycle (scan 05). They were closed after subsequent specimen unloading, while damage outside the notch region was still active. This trend was observed for all subsequent unloading stages. The reported results demonstrated that, despite high strain gradients induced in the notched region, the final failure of the investigated material was driven by the heterogeneous mesostructure, and thus the investigated material was notch-insensitive [29].

5. Conclusion

The present paper discussed the quantification of strain activity and damage growth within a single-notched specimen subjected to cyclic tensile loading. First, the major eigen strain fields and correlation residual maps were investigated. The former revealed the formation of a horizontal strained band extending through the whole ligament area from the very beginning of the loading history. The final crack path followed this early strained band. As the loading levels increased, multiple strained bands developed within the investigated specimen. They experienced an increase in strain levels, in spite of high strain gradients within the notched region. Furthermore, the first damaged zones appeared in the vicinity of the unnotched specimen ligament edge, and not in the notched region. Thus, the influence of specimen machining was proven herein. It is important to note that, compared to the notched region, damage in the remaining part of the ROI was more pronounced.

The strained band activity and damage growth were further quantified by studying cumulative probabilities of major eigen strain distributions. The change in the mean levels and standard deviations of the corresponding distributions were reported and analyzed. Std(ε_1) of the scans acquired in the loaded stages were significantly higher than those of scan 00, and thus were deemed trustworthy. By analyzing the increase of fluctuations, it was possible to track the accumulation of permanent strains, as well as the initiation and opening of mesocracks. It should also be emphasized that, even though mean major eigen strain levels were higher in the notched region, the standard deviations of the corresponding major eigen strain distributions were higher in the remainder of the ROI. All these observations explain the notch-insensitivity of the studied composite.

Acknowledgments

This work was performed within the FULLINSPECT project supported by the Croatian Science Foundation (UIP-2019-04-5460 Grant).This work was also partially supported by the French "Agence Nationale de la Recherche" through the "Investissements d'avenir" program (ANR10-EQPX-37 MATMECA Grant).

CRediT author statement

Ana Vrgoč: Software, Formal analysis, Conceptualization, Writing - Original Draft, Visualization
Zvonimir Tomičević: Conceptualization, Validation, Resources, Writing - Review and Editing, Supervision, Project administration
Benjamin Smaniotto: Investigation
François Hild: Software, Validation, Conceptualization, Writing - Review and Editing, Supervision

Appendix A

This appendix gathers the scanning parameters (Table A.1) as well as the analysis parameters employed in volumetric correlations (Table A.2).

References

[1] A. Khechai, A. Tati, B. Guerira, A. Guettala, P. M. Mohite, Strength degradation and stress analysis of composite plates with circular, square and rectangular notches using digital image correlation, Composite Structures 185 (2018) 699–715.

[2] A. Brunner, Identification of damage mechanisms in fiber-reinforced polymer-matrix composites with acoustic emission and the challenge of assessing structural integrity and service-life, Construction and Building Materials 173 (2018) 629–637.

[3] F. Cosmi, C. Ravalico, Threshold identification for micro-tomographic damage characterisation in a short-fibre-reinforced polymer, Strain 51 (2015) 171–179.

[4] F. Sket, A. Enfedaque, C. D. Lopez, C. González, J. M. Molina-Aldareguia, J. Llorca, X-ray computed tomography analysis of damage evolution in open hole carbon fiber-reinforced laminates subjected to in-plane shear, Composites Science and Technology 133 (2016) 40–50.

[5] H. Rolland, N. Saintier, P. Wilson, J. Merzeau, G. Robert, In situ x-ray tomography investigation on damage mechanisms in short glass fibre reinforced thermoplastics: Effects of fibre orientation and relative humidity, Composites Part B-engineering 109 (2017) 170–186.

[6] A. M. Ortiz-Morales, I. Hanhan, J. J. Solano, M. D. Sangid, Observing progressive damage in carbon fiber epoxy laminate composites via 3d in-situ x-ray tomography, Engineering Fracture Mechanics 246 (2021) 107626.

[7] A. Buljac, C. Jailin, A. Mendoza, J. Neggers, T. Taillandier-Thomas, A. Bouterf, B. Smaniotto, F. Hild, S. Roux, Digital volume correlation: Review of progress and challenges, Experimental Mechanics 58 (2018) 661–708.

[8] A. Buljac, V.-M. T. Navas, M. Shakoor, A. Bouterf, J. Neggers, M. Bernacki, P. Bouchard, T. Morgeneyer, F. Hild, On the calibration of elastoplastic parameters at the microscale via x-ray microtomography and digital volume correlation for the simulation of ductile damage, European Journal of Mechanics A-solids 72 (2018) 287–297.

[9] Z. Tomičević, A. Bouterf, R. Surma, F. Hild, Damage observation in glass fiber reinforced composites via μ-tomography, Materials Today: Proceedings 12 (2019) 185–191.

[10] R. Brault, A. Germaneau, J. Dupré, P. Doumalin, S. Mistou, M. Fazzini, In-situ analysis of laminated composite materials by x-ray micro-computed tomography and digital volume correlation, Experimental Mechanics 53 (2013) 1143–1151.

[11] B. Croom, H. Jin, B. E. Mills, J. Carroll, K. Long, J. A. Brown, X. Li, Damage mechanisms in elastomeric foam composites: Multiscale x-ray computed tomography and finite element analyses, Composites Science and Technology 169 (2019) 195–202.

[12] K. Wang, S. Pei, Y. Li, J. Li, D. Zeng, X. Su, X. Xiao, N. Chen, In-situ 3d fracture propagation of short carbon fiber reinforced polymer composites, Composites Science and Technology 182 (2019) 107788.

[13] Detecting damage initiation in short fiber composites via in-situ x-ray tomography and digital volume correlation, Composites Communications 22 (2020) 100524.

[14] S. Roux, F. Hild, P. Viot, D. Bernard, Three dimensional image correlation from X-Ray computed tomography of solid foam, Composites Part A-Applied Science and Manufacturing 39 (8) (2008) 1253–1265.

[15] J. Réthoré, J. Tinnes, S. Roux, J. Buffière, F. Hild, Extended three-dimensional digital image correlation (X3D-DIC), C. R. Mécanique 336 (2008) 643–649.

[16] H. Leclerc, J. Périé, S. Roux, F. Hild, Voxel-scale digital volume correlation, Experimental Mechanics 51 (4) (2011) 479–490.

[17] J. Réthoré, N. Limodin, J. Buffière, F. Hild, W. Ludwig, S. Roux, Digital volume correlation analyses of synchrotron tomographic images, The Journal of Strain Analysis for Engineering Design 46 (2011) 683–695.

[18] Z. Tomičević, J. Kodvanj, F. Hild, Characterization of the nonlinear behavior of nodular graphite cast iron via inverse identification. Analysis of uniaxial tests, European Journal of Mechanics - A/Solids 59 (2016) 330–343.

[19] A. Vrgoč, Z. Tomičević, B. Smaniotto, F. Hild, Application of different imaging techniques for the characterization of damage in fiber reinforced polymer, Composites Part A: Applied Science and Manufacturing (2021).

[20] A. Kak, M. Slaney, Principles of computerized tomographic imaging, IEEE Press, New York, 1988.

[21] A. Mendoza, J. Neggers, F. Hild, S. Roux, Complete mechanical regularization applied to digital image and volume correlation, Computer Methods in Applied Mechanics and Engineering 355 (2019) 27–43.

[22] Z. Tomičević, F. Hild, S. Roux, Mechanics-aided digital image correlation, The Journal of Strain Analysis for Engineering Design 48 (2013) 330 – 343.

[23] Z. Tomičević, F. Hild, S. Roux, Mechanics-aided digital image correlation, J. Strain Analysis 48 (2013) 330–343.

[24] H. Leclerc, J. Neggers, F. Mathieu, F. Hild, S. Roux, Correli 3.0 (2015). doi:IDDN.FR.001.520008.000.S.P.2015.000.31500.

[25] J. Rannou, N. Limodin, J. Réthoré, A. Gravouil, W. Ludwig, M. Baïetto, J. Buffière, A. Combescure, F. Hild, S. Roux, Three dimensional experimental and numerical multiscale analysis of a fatigue crack, Comp. Meth. Appl. Mech. Eng. 199 (2010) 1307–1325.

[26] H. Leclerc, J. Périé, F. Hild, S. Roux, Digital volume correlation: What are the limits to the spatial resolution?, Mech. & Indust. 13 (2012) 361–371.

[27] T. Taillandier-Thomas, S. Roux, T. Morgeneyer, F. Hild, Localized strain field measurement on laminography data with mechanical regularization, Nucl. Inst. Meth. Phys. Res. B 324 (2014) 70–79.

[28] A. Buljac, T. Taillandier-Thomas, L. Helfen, T. Morgeneyer, F. Hild, Evaluation of measurement uncertainties of digital volume correlation applied to laminography data, Journal of Strain Analysis for Engineering Design 53 (2018) 49–65.

[29] A. Vrgoč, Z. Tomičević, B. Smaniotto, F. Hild, Characterization of glass fiber reinforced polymer via digital volume correlation: Investigation of notch sensitivity, Under review (2022).

[30] G. Hallo, C. Lacombe, R. Parreault, N. Roquin, T. Donval, L. Lamaignère, J. Néauport, F. Hild, Sub-pixel detection of laser-induced damage and its growth on fused silica optics using registration residuals., Optics express 29 22 (2021) 35820–35836.

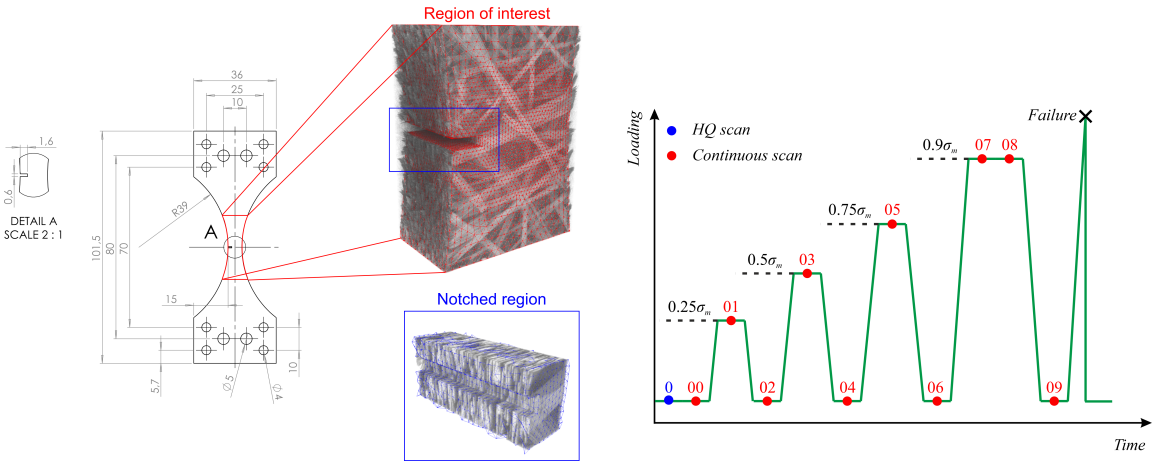

(a) **(b)**

Figure 1. (a) Geometry of the investigated single notched dogbone specimen together with the region of interest inspected in DVC analyses. The red contour depicts the region of interest, while the blue box denotes the notched region employed for quantification of strain activity and damage growth. The size of the region of interest was 680×465×1001 voxels, while the size of the notched region was 680×90×120 voxels. The physical length of one voxel was equal to 14.6 µm. (b) Schematic representation of loading and acquisition history of the *in-situ* tensile test. The first scan (0) was acquired in the unloaded state and was considered as the reference to evaluate measurement uncertainties and run subsequent correlations. Then, 10 additional scans were acquired for the purpose of *in-situ* bulk kinematic measurements.

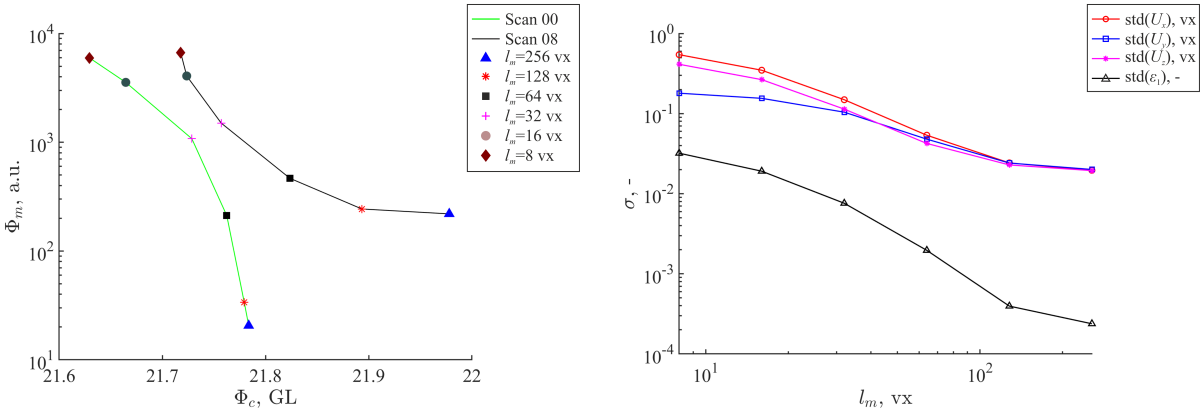

(a) **(b)**

Figure 2. (a) Change of mechanical residuals Φ_m with respect to gray level correlation residuals Φ_c for scans 00 and 08. (b) Standard displacement and nodal major eigen strain uncertainties for different bulk regularization lengths ℓ_m.

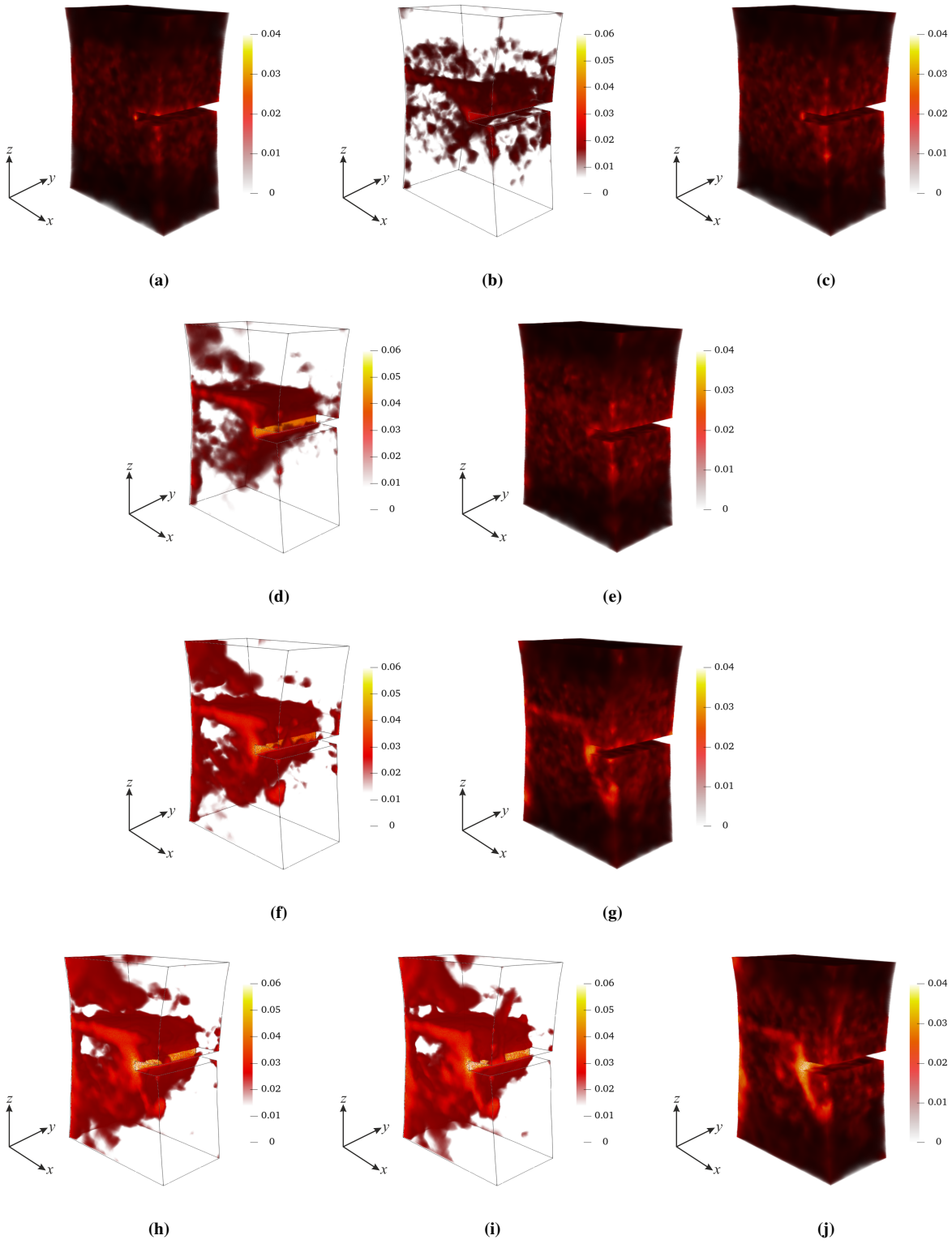

Figure 3. Thresholded major eigen strain fields of the single notched specimen computed for scans (a) 00, (b) 01, (c) 02, (d) 03, (e) 04, (f) 05, (g) 06, (h) 07, (i) 08 and (j) 09.

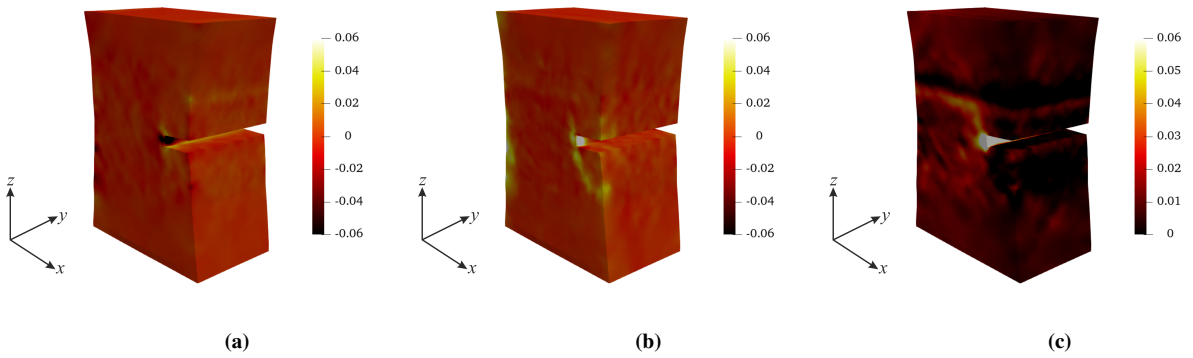

Figure 4. 3D renderings of ε_{xx}, ε_{yy} and ε_{zz} strain fields for scan 08.

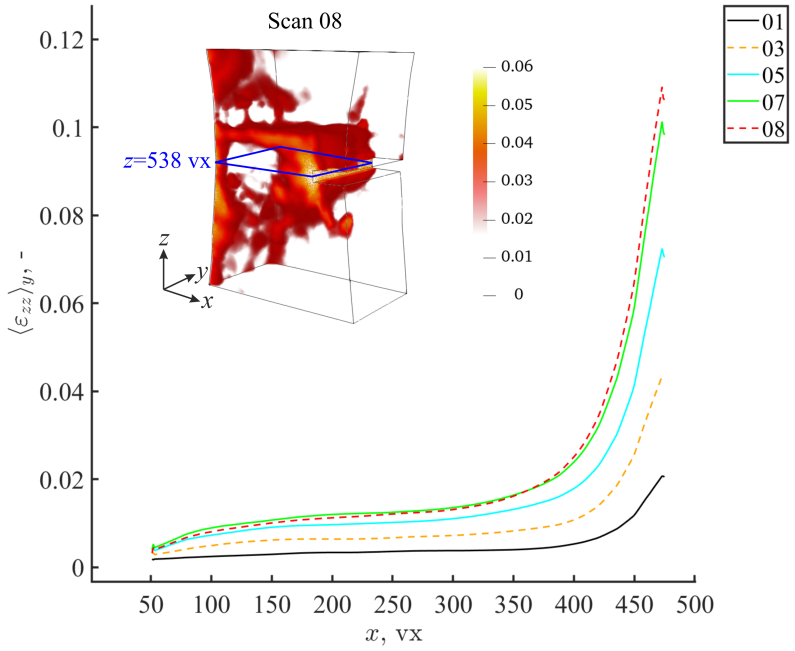

Figure 5. ε_{zz} strains averaged through the material thickness ($y-$direction) and extracted for the mid-height notch plane ($z = 538$ vx). The averaged ε_{zz} strains were computed for the scans acquired at the peak of the prescribed loading cycles (*i.e.*, scans 01, 03, 05, 07 and 08). The blue rectangle in the thresholded ε_{zz} field of scan 08 depicts the plane in which the through-thickness averaged ε_{zz} strains were assessed.

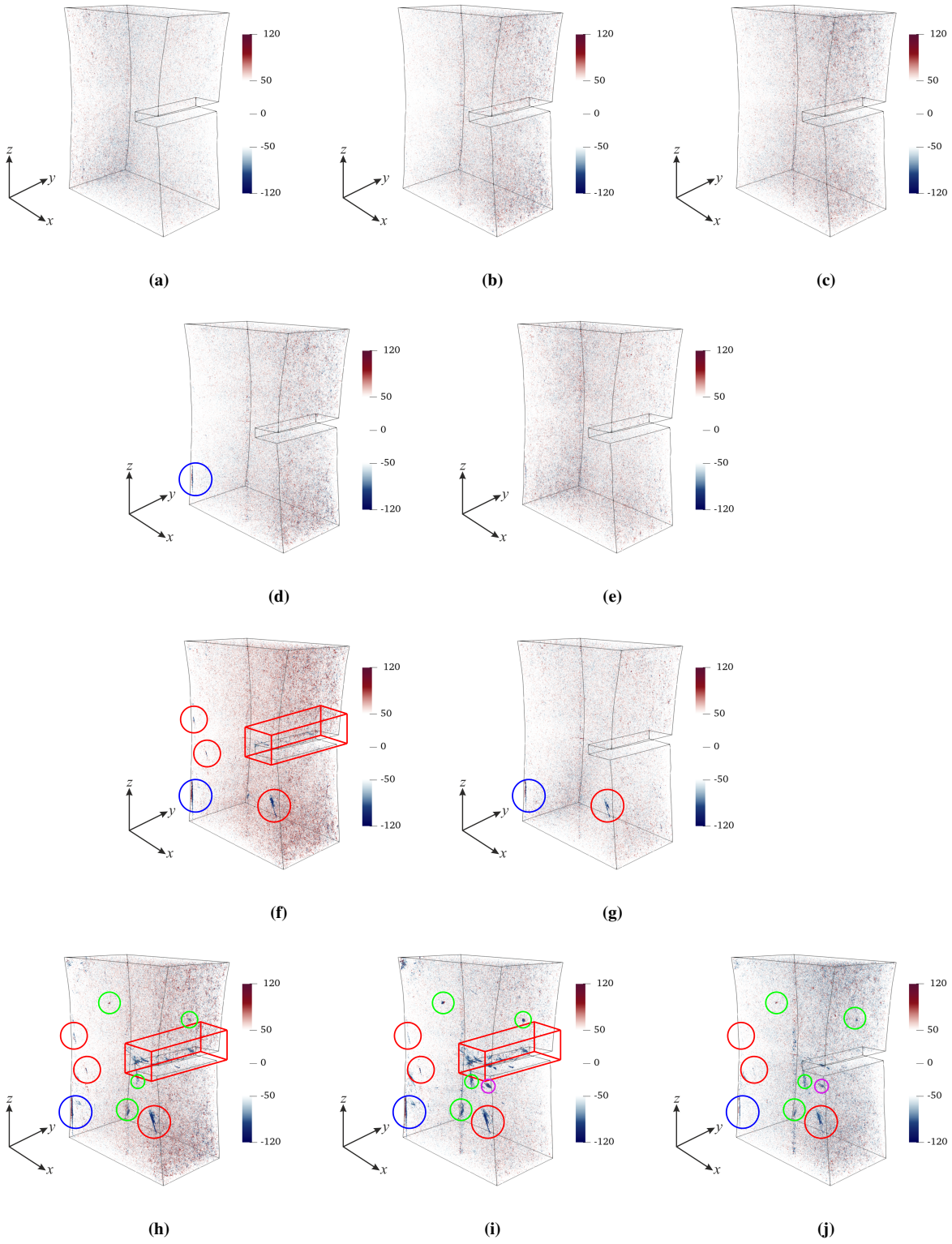

Figure 6. Gray level residual maps of the single notched specimen calculated for scans (a) 00, (b) 01, (c) 02, (d) 03, (e) 04, (f) 05, (g) 06, (h) 07, (i) 08 and (j) 09. The blue circles depict the first detected damage locations, while the red, green and purple circles indicate additional damaged zones. The red rectangular prism denotes damaged zones in the notched region.

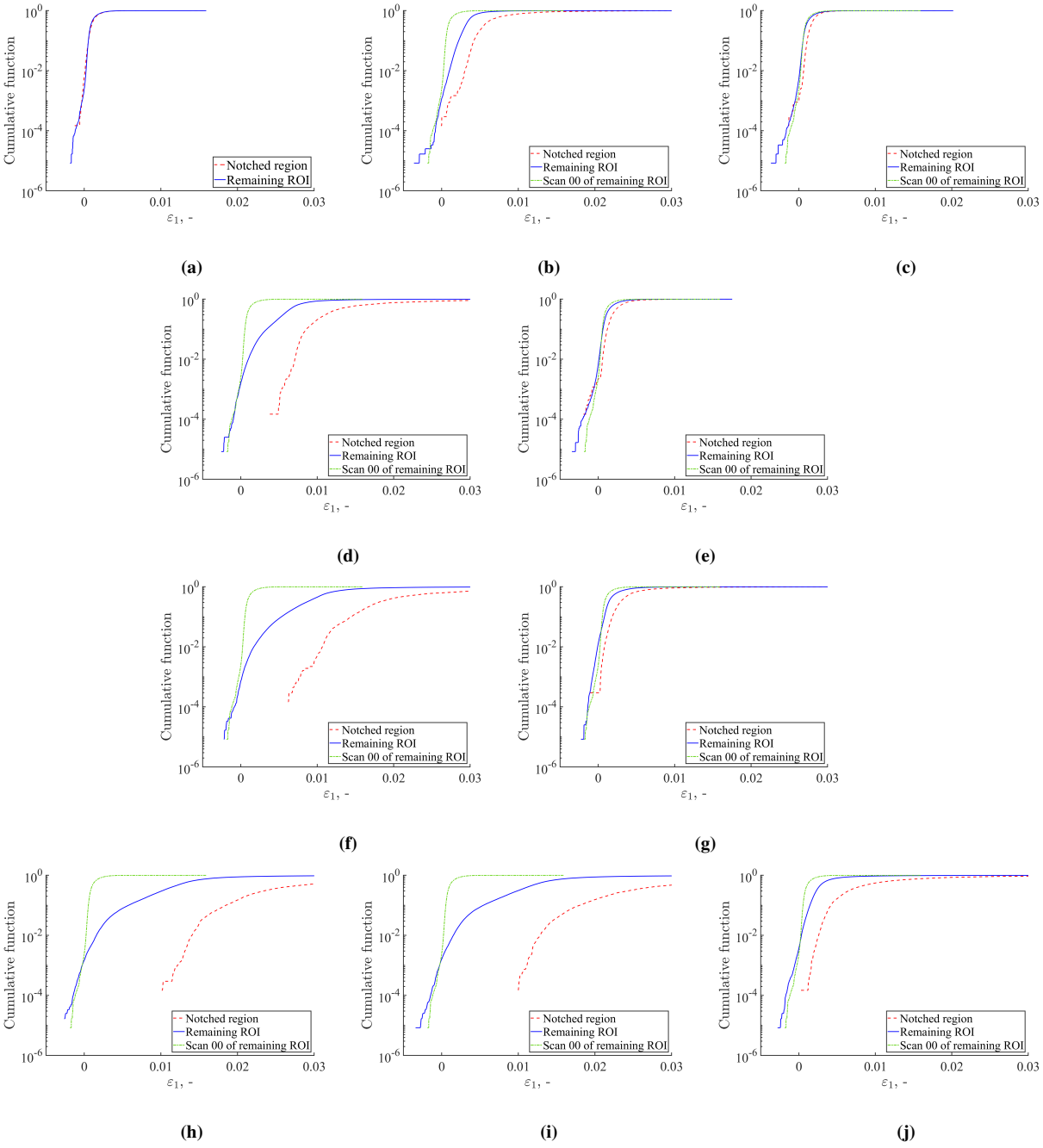

Figure 7. Comparison of cumulative probabilities of major eigen strains of the notched region and the remainder of the inspected ROI (Fig. 1(a)) for scans (a) 00, (b) 01, (c) 02, (d) 03, (e) 04, (f) 05, (g) 06, (h) 07, (i) 08 and (j) 09.

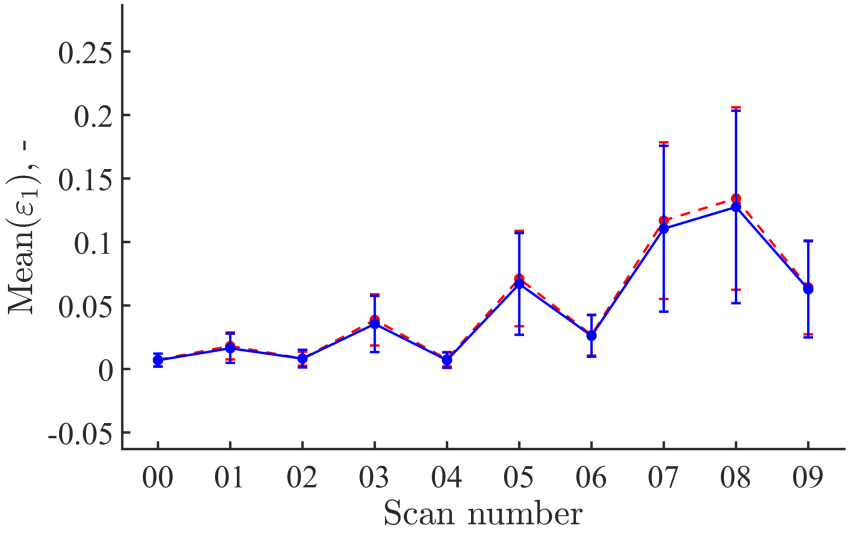

Figure 8. Comparison of mean levels of major eigen strain distributions between the notched region and the remainder of the ROI (Fig. 1(a)). The error bars depict the standard deviation of the corresponding distributions.

Table 1: Standard displacement and strain uncertainties of DVC measurements, as well as RMS norm of the correlation residuals when employing bulk and surface regularization length equal to 64 vx. The measurement uncertainties were evaluated by correlating the two scans acquired prior to prescribing tension (*i.e.*, scans 0 and 00, see Fig. 1(b)).

Std(U_x)	0.05 vx
Std(U_y)	0.05 vx
Std(U_z)	0.04 vx
Std(ε_1)	5×10^{-4}
RMS($\boldsymbol{\varphi_c}$)	21.7 GL

Table 2: Mean level and standard deviation of major eigen strain distributions extracted for the prescribed loading history.

Scan	Mean(ε_1), -		Std(ε_1), -	
	Remaining ROI	Notched region	Remaining ROI	Notched region
00	0.007	0.007	0.005	0.005
01	0.016	0.018	0.011	0.010
02	0.007	0.008	0.006	0.006
03	0.035	0.038	0.023	0.021
04	0.008	0.009	0.006	0.006
05	0.067	0.071	0.041	0.037
06	0.023	0.027	0.016	0.012
07	0.114	0.121	0.065	0.062
08	0.127	0.134	0.076	0.072
09	0.062	0.064	0.037	0.032

Table A.1: Scanning parameters.

Tomograph	North Star Imaging X50+	
X-ray source	XRayWorX XWT-240-CT	
Target/ Anode	W (reflection mode)	
Filter	None	
Voltage	145 kV	
Current	78 µA	
Focal spot size	5 µm	
Tube to detector	910 mm	
Tube to object	53 mm	
Detector	Dexela 2923	
Definition	1507 × 1849 pixels (2 × 2 binning)	
Scanning settings	High quality	Continuous
Number of projections	800	768
Angular amplitude	360°	360°
Frame average	20 per projection	Continuous (1 per step)
Frame rate	3 fps	3 fps
Acquisition duration	1 h 46 min 26 s	4 min 26 s
Reconstruction algorithm	Filtered back-projection	Filtered back-projection
Gray level amplitude	8 bits	8 bits
Volume size	680×465×1001 vx (after crop)	680×465×1001 vx (after crop)
Field of view	7.3 × 10 × 20.5 mm^3	7.3 × 10 × 20.5 mm^3
Image scale	14.6 µm/voxel	14.6 µm/voxel

Table A.2: DVC analysis parameters employed herein.

DVC software	Correli 3.0 [24]
Image filtering	None
Element length (mean)	11 vx
Shape functions	Linear (T4)
Mesh	Unstructured (Fig. 1(a))
Matching criterion	Penalized sum of square differences
Regularization length	Bulk: 64 vx, Dirichlet nodes: 64 vx
Interpolant	Cubic